*J. Fluid Mech.* (2006), *vol.* 555, *pp.* 177–202.  
doi:10.1017/S0022112006008858 Printed in the United Kingdom

# Nonlinear development of oscillatory instability in a two-layer system under the combined action of buoyancy and thermocapillary effect

By ILYA B. SIMANOVSKII
AND ALEXANDER A. NEPOMNYASHCHY

Department of Mathematics, Technion – Israel Institute of Technology, 32000 Haifa, Israel

(Received 25 January 2005 and in revised form 26 October 2005)

The oscillatory convection for a real system of fluids under the joint action of buoyancy and thermocapillary effect is investigated. The nonlinear development of the oscillatory instability is studied. Two types of boundary condition are considered. In the case of periodic boundary conditions, regimes of either travelling waves or standing oscillations have been found, depending on the period of the flow. For rigid heat-insulated lateral walls, various types of symmetric and asymmetric standing waves are obtained. Transitions between the motions with different spatial structures are investigated. It is shown that in the case of rigid heat-insulated lateral walls the period of oscillations changes non-monotonically. The nonlinear oscillations exist in a finite interval of the Grashof number values, between the stability regions of a quiescent state and stationary convection.

## 1. Introduction

The phenomenon of Rayleigh–Bénard convection in two-layer systems has been studied extensively during the last few decades (see Simanovskii & Nepomnyashchy 1993; Colinet, Legros & Velarde 2001). In the case, when the 'local' Rayleigh numbers determined by the parameters of the corresponding layer differ considerably, an intensive convective motion arises only in one fluid and a weak induced motion takes place in the second layer (Simanovskii 1979). If the Rayleigh numbers are close, heat and hydrodynamic interactions on the interface play the dominant role. The situation with close values of the local Rayleigh numbers was considered first by Busse (1981). Two monotonic instability modes, corresponding to the onset of convection in each fluid layer, have been found. However, the eigenvalues of the linear stability problem can be complex in the case of a two-layer system, because the stability problem is not self-adjoint (Simanovskii & Nepomnyashchy 1993). Hence, an oscillatory instability is possible in general. Gershuni & Zhukhovitsky (1982) have found a real system (the transformer oil–formic acid system) such that in a certain interval of the wavenumbers, an oscillatory instability was predicted by the stability analysis. However, the threshold value of the Rayleigh number for the oscillatory instability was higher than that for the monotonic instability (which took place in other intervals of wavenumbers). Therefore, the predicted instability could not be observed in experiments.

In order to diminish the oscillatory threshold below the monotonic one, some 'artificial' systems have been suggested (Gilev, Nepomnyashchy & Simanovskii 1987; Rasenat, Busse & Rehberg 1989; Renardy 1996). The nonlinear oscillatory convective

structures near the instability threshold have been studied by Colinet & Legros (1994) and Renardy, Renardy & Fujimura (1999). Let us emphasize, that the oscillatory instability was not predicted for any real system of fluids, because the critical Rayleigh number for the oscillatory instability was always higher than that for the monotonic instability.

Nevertheless, the oscillations just above the instability threshold have been observed in the experiments of Degen, Colovas & Andereck (1998). It should be noted that the linear stability theory for the onset of the buoyancy convection has predicted a monotonic instability (Nepomnyashchy & Simanovskii 2004). The appearance of the oscillations might be caused by the influence of the thermocapillary effect (Liu, Zhou & Tang 2004; Nepomnyashchy & Simanovskii 2004).

In the present paper, we investigate the nonlinear regimes of the oscillatory convection for a real system of fluids. As the top-layer fluid, we choose 2cS silicone oil, Rhone Poulenc's Rhodorsil 47v2, used in the experiments of Degen *et al.* (1998); water is taken as the bottom-layer fluid. The influence of the thermocapillary effect on the thermogravitational oscillations is taken into account. Attention is paid mainly to the transitions between the motions with different spatial structures. In the case of periodic boundary conditions, regimes of travelling waves and standing oscillations have been obtained. In the case of rigid lateral walls, regimes of symmetric and asymmetric oscillations have been found. It is shown that the region of the Grashof number values, where nonlinear oscillations take place, is bounded both from below (by the mechanical equilibrium state) and from above (by the steady state).

The paper is organized as follows. In § 2, the mathematical formulation of the problem is presented and the nonlinear approach is described. In § 3, the influence of the thermocapillary effect on the oscillatory mode of instability is studied. Nonlinear simulations of oscillatory flow regimes are considered. Section 4 contains some concluding remarks.

## 2. Formulation of the problem

### 2.1. *Equations and boundary conditions*

We consider a system of two horizontal layers of immiscible viscous fluids with different physical properties. The system is bounded from above and from below by two isothermic rigid plates kept at constant different temperatures (the total temperature drop is $\theta$). It is assumed that the interfacial tension $\sigma$ decreases linearly with the increase in the temperature: $\sigma = \sigma_0 - \alpha T$, where $\alpha > 0$.

The variables referring to the top layer are marked by subscript 1, and the variables referring to the bottom layer by subscript 2.

Assume that $\rho_m$, $\nu_m$, $\eta_m$, $\kappa_m$, $\chi_m$, $\beta_m$ and $a_m$ are, respectively, density, kinematic and dynamic viscosity, heat conductivity, thermal diffusivity, thermal expansion coefficient and the thickness of the $m$th layer ($m = 1, 2$). Let us introduce the following non-dimensional parameters, corresponding to parameter ratios of different fluids,

$$\rho = \rho_1/\rho_2, \qquad \nu = \nu_1/\nu_2, \qquad \eta = \eta_1/\eta_2,$$
$$\kappa = \kappa_1/\kappa_2, \qquad \chi = \chi_1/\chi_2, \qquad \beta = \beta_1/\beta_2,$$

and to the ratio of layers thicknesses,

$$a = a_2/a_1.$$

As the units of length, time, velocity, pressure and temperature we choose $a_1$, $a_1^2/\nu_1$, $\nu_1/a_1$, $\rho_1\nu_1^2/a_1^2$ and $\theta$, respectively.

The nonlinear equations of convection in the framework of the Boussinesq approximation for both fluids have the following form (see Simanovskii & Nepomnyashchy 1993):

$$\frac{\partial \boldsymbol{v}_m}{\partial t} + (\boldsymbol{v}_m \cdot \nabla)\boldsymbol{v}_m = -e_m \nabla p_m + c_m \nabla^2 \boldsymbol{v}_m + b_m G T_m \boldsymbol{\gamma}, \tag{1a}$$

$$\frac{\partial T_m}{\partial t} + \boldsymbol{v}_m \cdot \nabla T_m = \frac{d_m}{P} \nabla^2 T_m, \tag{1b}$$

$$\nabla \cdot \boldsymbol{v}_m = 0. \tag{1c}$$

Here, $\boldsymbol{v}_m = (v_{mx}, v_{my}, v_{mz})$ is the velocity vector, $T_m$ is the temperature and $p_m$ is the pressure in the $m$th fluid; $\boldsymbol{\gamma}$ is the unit vector directed upwards; $b_1 = c_1 = d_1 = e_1 = 1$; $b_2 = 1/\beta$, $c_2 = 1/\nu$, $d_2 = 1/\chi$, $e_2 = \rho$; $G = g\beta_1 \theta a_1^3/\nu_1^2$ is the Grashof number, which characterizes the buoyancy force, and $P = \nu_1/\chi_1$ is the Prandtl number for the liquid in layer 1. The conditions on the isothermic rigid horizontal boundaries are:

$$z = 1 + a: \quad \boldsymbol{v}_1 = 0, \quad T_1 = 0, \tag{2}$$

$$z = 0: \quad \boldsymbol{v}_2 = 0, \quad T_2 = 1. \tag{3}$$

In order to be compatible with the system of equations (1), we assume that the interface is flat, and it is located at $z = 0$. Indeed, the balance of normal stresses on the interface shows that the interface deformation is proportional to $1/Ga\delta$ (Simanovskii & Nepomnyashchy 1993) where the Galileo number $Ga = ga_1^3/\nu_1^2$ determines the ratio of the gravity and viscous forces, and the coefficient $\delta = \rho^{-1} - 1$ characterizes the difference between fluids densities. However, the Boussinesq approximation is based on the assumption $\epsilon_\beta = \beta_1 \theta \ll 1$, $G = O(1)$, therefore the Galileo number $Ga = G/\epsilon_\beta \gg 1$. Because $1/Ga\delta = \epsilon_\beta / G\delta$ is small unless $\delta \ll 1$, we conclude that in the framework of the Boussinesq approximation, the interfacial deformation must be neglected, if the densities of the fluids are not close to each other. (The case of close densities is not considered in the present paper).

The boundary conditions on the interface include relations for the tangential stresses:

$$z = a: \quad \eta \frac{\partial v_{1x}}{\partial z} = \frac{\partial v_{2x}}{\partial z} + \frac{\eta M}{P} \frac{\partial T_1}{\partial x}, \quad \eta \frac{\partial v_{1y}}{\partial z} = \frac{\partial v_{2y}}{\partial z} + \frac{\eta M}{P} \frac{\partial T_2}{\partial x}; \tag{4}$$

the continuity of the velocity field:

$$v_1 = v_2; \tag{5}$$

the continuity of the temperature field:

$$T_1 = T_2; \tag{6}$$

and the continuity of the heat flux normal components:

$$\kappa \frac{\partial T_1}{\partial z} - \frac{\partial T_2}{\partial z} = 0. \tag{7}$$

Here, $M = \alpha \theta a_1 / \eta_1 \chi_1$ is the Marangoni number, which is the basic non-dimensional parameter characterizing the thermocapillary effect.

The problem (1)–(7) for any choice of parameters has the solution:

$$\boldsymbol{v}_m^0 = 0, \qquad p_m = p_m^0(z), \qquad T_m = T_m^0(z) \qquad (m = 1, 2), \tag{8}$$

corresponding to the quiescent state. The temperature gradients in the quiescent state are:

$$A_1 = \mathrm{d}T_1^0/\mathrm{d}z = -\frac{1}{(1+\kappa a)}, \quad A_2 = \mathrm{d}T_2^0/\mathrm{d}z = -\frac{\kappa}{(1+\kappa a)}. \tag{9}$$

Recall that in the case of a buoyancy convection in a one-layer system, the monotonic instability threshold is determined by the Rayleigh number $R = GP$ rather than by the Grashof number $G$. Therefore, in the case $M = 0$, it is convenient to define the 'local' Rayleigh numbers

$$R_m = \frac{g\beta_m |\bar{A}_m| a_m^4}{\nu_m \chi_m} \qquad (m = 1, 2), \tag{10}$$

which are constructed using the parameters of the corresponding fluids ($\bar{A}_m$ is the dimensional temperature gradient in the $m$th fluid). The values of $R_m$ are connected with the non-dimensional parameters in the following way:

$$R_1 = \frac{GP}{1+\kappa a}, \quad R_2 = \frac{GP\kappa}{1+\kappa a}\frac{\nu\chi a^4}{\beta}. \tag{11}$$

The ratio of local Rayleigh numbers,

$$r = \frac{R_2}{R_1} = \frac{\kappa\nu\chi a^4}{\beta}, \tag{12}$$

depends on the physical properties of both fluids as well as on the ratio of thicknesses $a$.

In the case when the local Rayleigh numbers are essentially different from each other ($r \gg 1$ or $r \ll 1$), we can easily distinguish between neutral stability curves which correspond to the onset of convection in different layers. When the local Rayleigh numbers are close, we can observe a mode mixing and the appearance of an oscillatory instability, if the linearized eigenvalue problem is not self-adjoint; i.e. if $\eta\beta\chi/\nu \neq 1$ or $M \neq 0$ (see Simanovskii & Nepomnyashchy 1993).

### 2.2. *Numerical approach*

In order to investigate the flow regimes generated by the convective instabilities, we perform nonlinear simulations of two-dimensional flows ($v_{my} = 0$ $(m = 1, 2)$; the fields of physical variables do not depend on $y$). In this case, we can introduce the streamfunction $\psi$

$$v_{mx} = \frac{\partial\psi_m}{\partial z}, \quad v_{mz} = -\frac{\partial\psi_m}{\partial x} \qquad (m = 1, 2).$$

Eliminating the pressure and defining the vorticity

$$\phi_m = \frac{\partial v_{mz}}{\partial x} - \frac{\partial v_{mx}}{\partial z},$$

we can rewrite the boundary-value problem (1)–(7) in the following form:

$$\frac{\partial\phi_m}{\partial t} + \frac{\partial\psi_m}{\partial z}\frac{\partial\phi_m}{\partial x} - \frac{\partial\psi_m}{\partial x}\frac{\partial\phi_m}{\partial z} = c_m\nabla^2\phi_m + b_m G\frac{\partial T_m}{\partial t}, \tag{13}$$

$$\nabla^2\psi_m = -\phi_m, \tag{14}$$

$$\frac{\partial T_m}{\partial t} + \frac{\partial\psi_m}{\partial z}\frac{\partial T_m}{\partial x} - \frac{\partial\psi_m}{\partial x}\frac{\partial T_m}{\partial z} = \frac{d_m}{P}\nabla^2 T_m \qquad (m = 1, 2). \tag{15}$$

$$z = 1 + a: \quad \psi_1 = \frac{\partial\psi_1}{\partial z} = 0, \quad T_1 = 0; \tag{16}$$

$$z = 0: \quad \psi_2 = \frac{\partial \psi_2}{\partial z} = 0, \quad T_2 = 1; \tag{17}$$

$$z = a: \quad \psi_1 = \psi_2 = 0, \quad \frac{\partial \psi_1}{\partial z} = \frac{\partial \psi_2}{\partial z}, \quad \phi_2 = \eta \phi_1 + \frac{\eta M}{P} \frac{\partial T_1}{\partial x}; \tag{18}$$

$$T_1 = T_2, \quad \kappa \frac{\partial T_1}{\partial z} = \frac{\partial T_2}{\partial z}. \tag{19}$$

The coefficients $b_m$, $c_m$ and $d_m$ have been defined in § 2.1.

The calculations were performed in a finite region $0 \leqslant x \leqslant L$, $-a \leqslant z \leqslant 1$ with the following types of boundary conditions on the lateral boundaries:

(i) periodic boundary conditions:

$$\psi_m(x + L, z) = \psi_m(x, z); \quad \phi_m(x + L, z) = \phi_m(x, z); \quad T_m(x + L, z) = T_m(x, z); \tag{20}$$

(ii) rigid heat-insulated boundaries:

$$x = 0, L: \quad \psi_m = \frac{\partial \psi_m}{\partial x} = \frac{\partial T_m}{\partial x} = 0 \qquad (m = 1, 2). \tag{21}$$

The boundary conditions (i) correspond to spatially periodic structures in a laterally infinite two-layer system; the boundary conditions (ii) correspond to a closed cavity. The problem (13)–(20) or (13)–(19), (21) is integrated in time with some initial conditions for $\psi_m$ and $T_m$ ($m = 1, 2$) by means of a finite-difference method. Equations and boundary conditions are approximated on a uniform mesh using a second-order approximation for the spatial coordinates. The nonlinear equations are solved using an explicit scheme on a rectangular uniform mesh $56 \times 56$ ($L = 2.74$), and $168 \times 56$ ($L = 16$). The Poisson equation is solved by the iterative Liebman successive over-relaxation method on each time step; the accuracy of the solution is $10^{-5}$. Kuskova & Chudov (1968) formulae, providing the second-order accuracy, are used for the approximation of the vorticity on the solid boundaries.

At the interface, the expression for the vorticity is approximated with the second-order accuracy for the spatial coordinates and have a form:

$$\phi_1 = \frac{-2[\psi_2(x, a - \Delta z) + \psi_1(x, a + \Delta z)]}{(\Delta z)^2 (1 + \eta)}, \tag{22}$$

$$\phi_2(x, a) = \eta \phi_1(x, a). \tag{23}$$

Here, $\Delta x$, $\Delta z$ are the mesh sizes for the corresponding coordinates. The temperatures on the interfaces are calculated by the second-order approximation formulae:

$$T_1(x, a) = T_2(x, a) = \frac{[4T_2(x, a - \Delta z) - T_2(x, a - 2\Delta z)] + \kappa[4T_1(x, a + \Delta z) - T_1(x, a + 2\Delta z)]}{3(1 + \kappa)}. \tag{24}$$

## 3. Generation of oscillations

We investigate the onset of the Rayleigh–Bénard convection in the 47v2 silicone oil–water system with the following set of parameters: $\nu = 2.0$; $\eta = 1.7375$; $\kappa = 0.184$; $\chi = 0.778$; $\beta = 5.66$; $P = 25.7$. This system was used in experiments on the convection in two-layer systems carried out by Degen *et al.* (1998). For the system under consideration, the value of the 'non-self-adjointness parameter' $\eta\beta\chi/\nu = 3.83$ is rather far from 1, which is favourable for the appearance of an oscillatory instability.

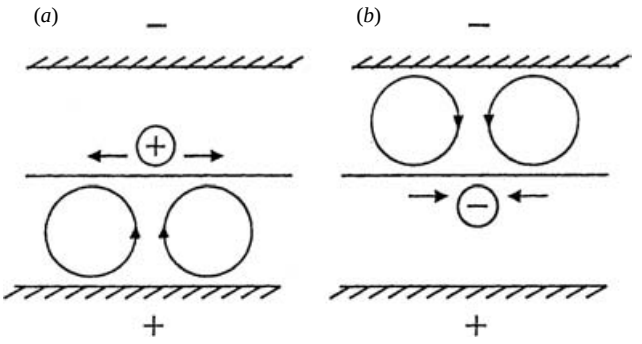


FIGURE 1. Interaction between buoyancy and thermocapillarity. (*a*) The buoyancy convection is in the bottom layer. (*b*) The buoyancy convection is in the top layer.

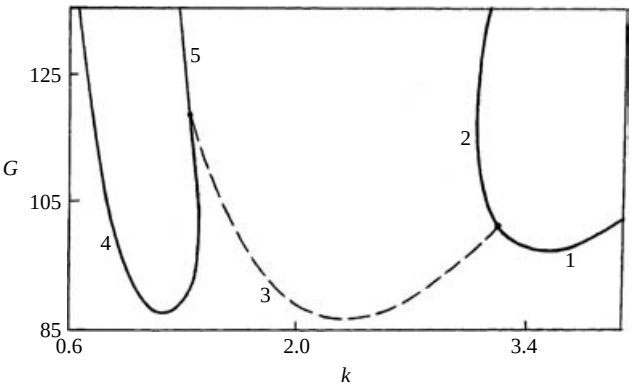


FIGURE 2. The neutral curves for $a = 1.6$; $K = 0.4$.

The goal of the present nonlinear simulations is to find typical stable oscillatory flow regimes. The analysis does not pretend to give a description of the full bifurcation diagram for the complex nonlinear system (13)–(20) or (13)–(19), (21).

The discretized nonlinear problem is a dynamical system with a very large number of variables. Nevertheless, the attractors observed in simulations are low-dimensional.

### 3.1. *Infinite layers*

We shall start our analysis by considering the case of infinite layers, where we can use predictions of the linear theory (Nepomnyashchy & Simanovskii 2004). The computations are carried out with periodic boundary conditions (20).

#### 3.1.1. *Predictions of the linear theory*

Substituting the physical parameters of the system into relation (12), we find that $r = 0.05a^4$. Thus, $r = 1$ as $a = a_* = 2.1$.

First, let us consider the case, corresponding to 'pure' buoyancy convection ($M = 0$). If $r < 1$ ($r > 1$), the monotonic instability of the mechanical equilibrium state generates an intensive convective motion in the top (bottom) layer and a relatively weak motion in the bottom (top) layer.

However, in the case $r \approx 1$, i.e. $a \approx a_*$, two instability modes, corresponding to the onset of convection in each layer, determine two minima of monotonic instability curves located at essentially different values of the wavenumber. For the intermediate values of the wavenumber, an oscillatory instability takes place, which is caused by

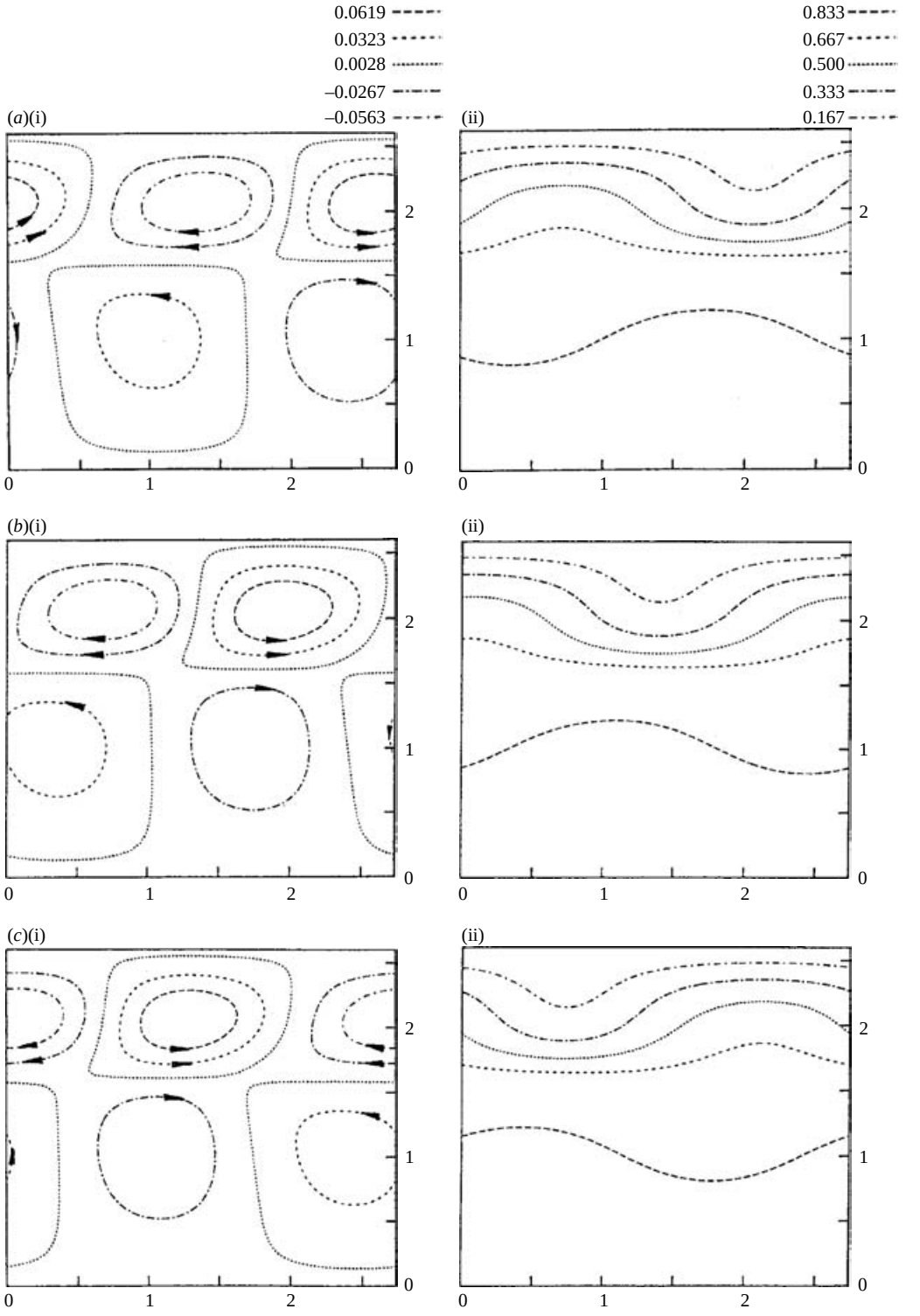


FIGURE 3. Snapshots of ($a$(i) – $c$(i)) streamlines and ($a$(ii) – $c$(ii)) isotherms for the travelling wave at $a = 1.6$; $L = 2.74$; $G = 100$; $K = 0.4$; ($a$) $t = 0$; ($b$) $t = \tau/4$; ($c$) $t = \tau/2$, where $\tau$ is the period. The wave moves from the right- to the left-hand side.

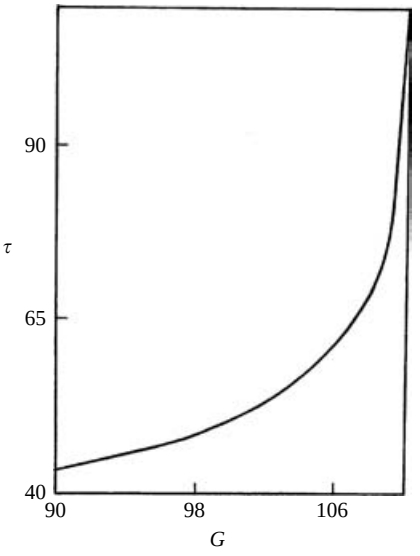


FIGURE 4. The dependence of the period of oscillations on the Grashof number.

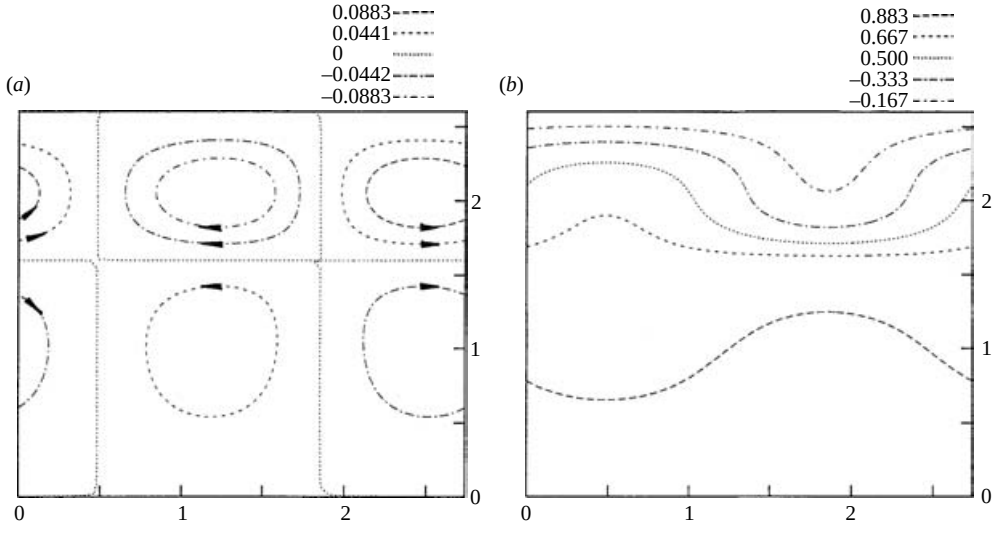


FIGURE 5. (*a*) Streamlines and (*b*) isotherms for the steady state ($G = 112$); $L = 2.74$.

the hydrodynamic and thermal interaction between convective motions on both sides of the interface.

Let us emphasize that for any values of $a$, the minimum of the neutral curve does not correspond to an oscillatory instability. No oscillatory regimes of convection have been obtained in nonlinear simulations with $M = 0$ (see Nepomnyashchy & Simanovskii 2004).

Let us discuss now the case of the combined action of the thermocapillary effect and the buoyancy. In the case $r > 1$, where the buoyancy convection takes place mainly in the bottom layer, a temperature disturbance on the interface generates buoyancy volume forces and thermocapillary tangential stresses acting in the same

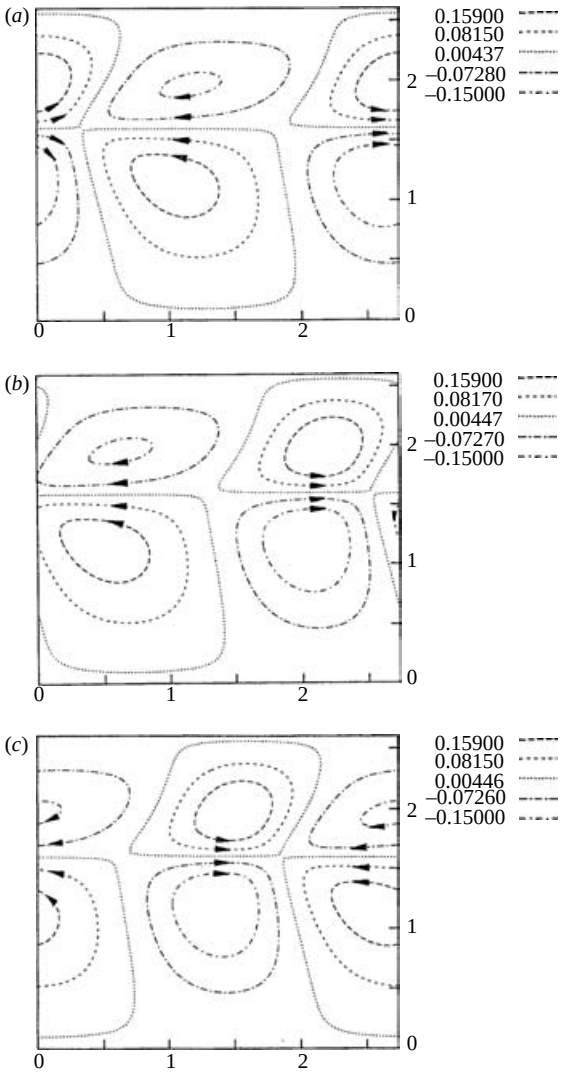


FIGURE 6. Snapshots of streamlines for the travelling wave at $G = 125$, $K = 5.75$, $L = 2.74$. (*a*) $t = 0$; (*b*) $t = \tau/4$; (*c*) $t = \tau/2$, where $\tau$ is the period. The wave moves from the right- to the left-hand side.

direction (see figure 1*a*). In this case, the action of the thermocapillary effect leads to a decrease of the minimized critical Grashof number. In the opposite case $r < 1$, where the buoyancy convection arises first in the top layer, the buoyancy volume forces and thermocapillary tangential stresses act in the opposite way (see figure 1*b*). The asynchronic action of two factors working in the opposite direction can produce an overstability.

Under the conditions of the experiment, when the geometric configuration of the system is fixed while the temperature difference $\theta$ is changed, the Marangoni number $M$ and the Grashof number $G$ are proportional. Define the inverse dynamic Bond number

$$K = \frac{M}{GP} = \frac{\alpha}{g\beta_1\rho_1 a_1^2}.$$

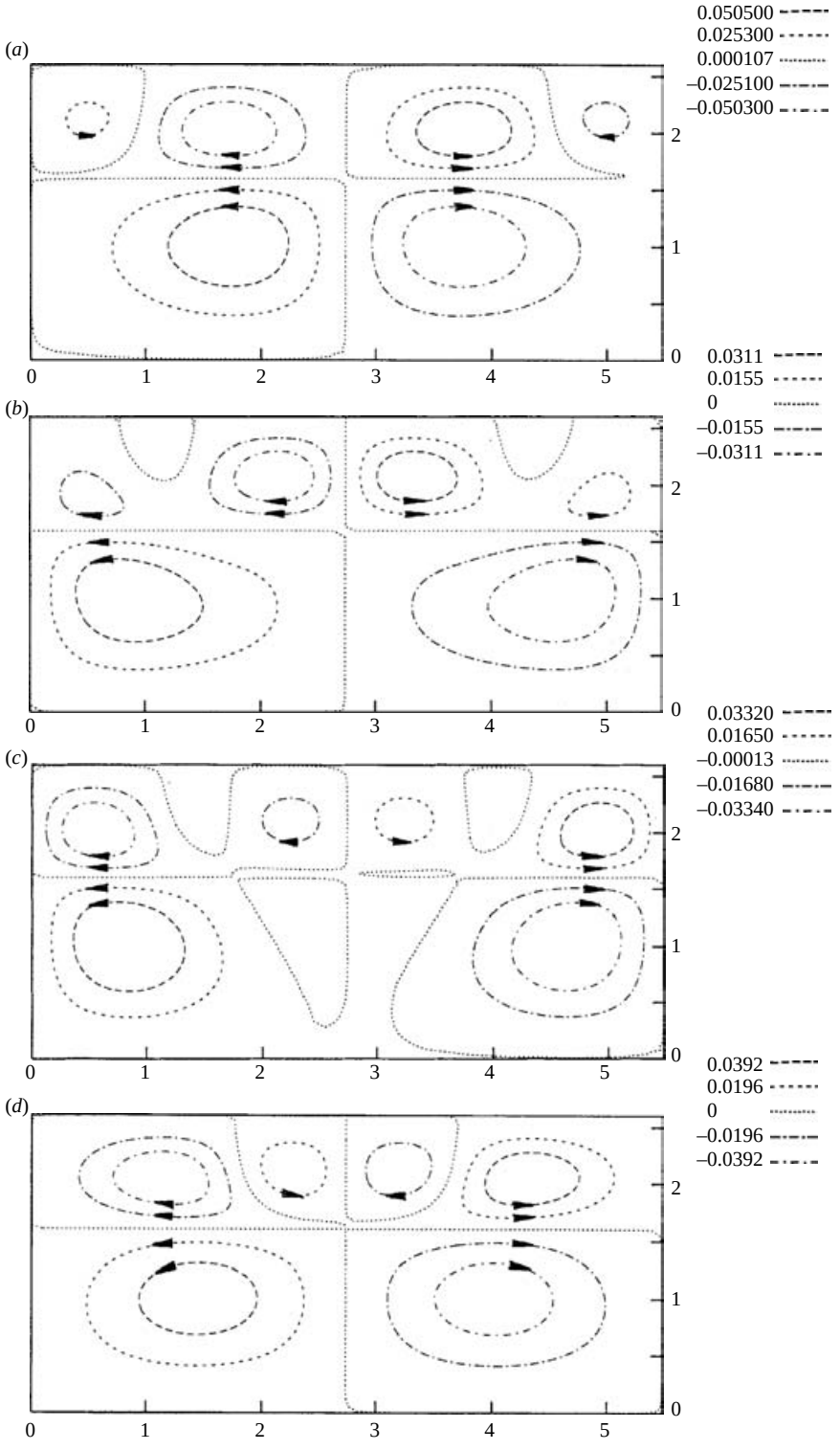


FIGURE 7(*a–d*). A time sequence of snapshots of streamlines for the symmetric oscillatory flow at $G = 89$, $K = 0.365$, $L = 5.48$.

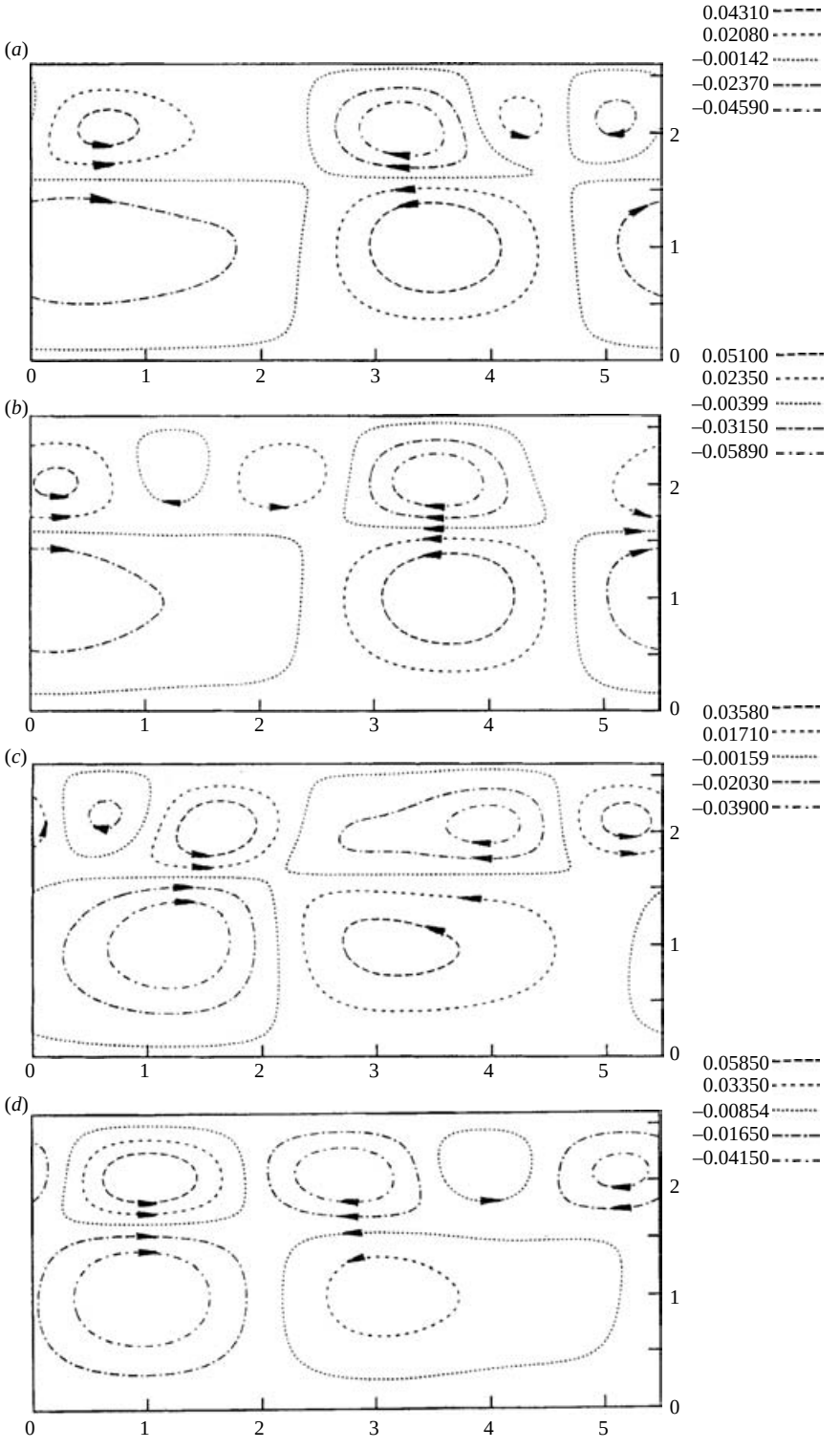


FIGURE 8(*a–d*). A time sequence of snapshots of streamlines for the asymmetric oscillatory flow at $G = 89$, $K = 0.365$, $L = 5.48$.

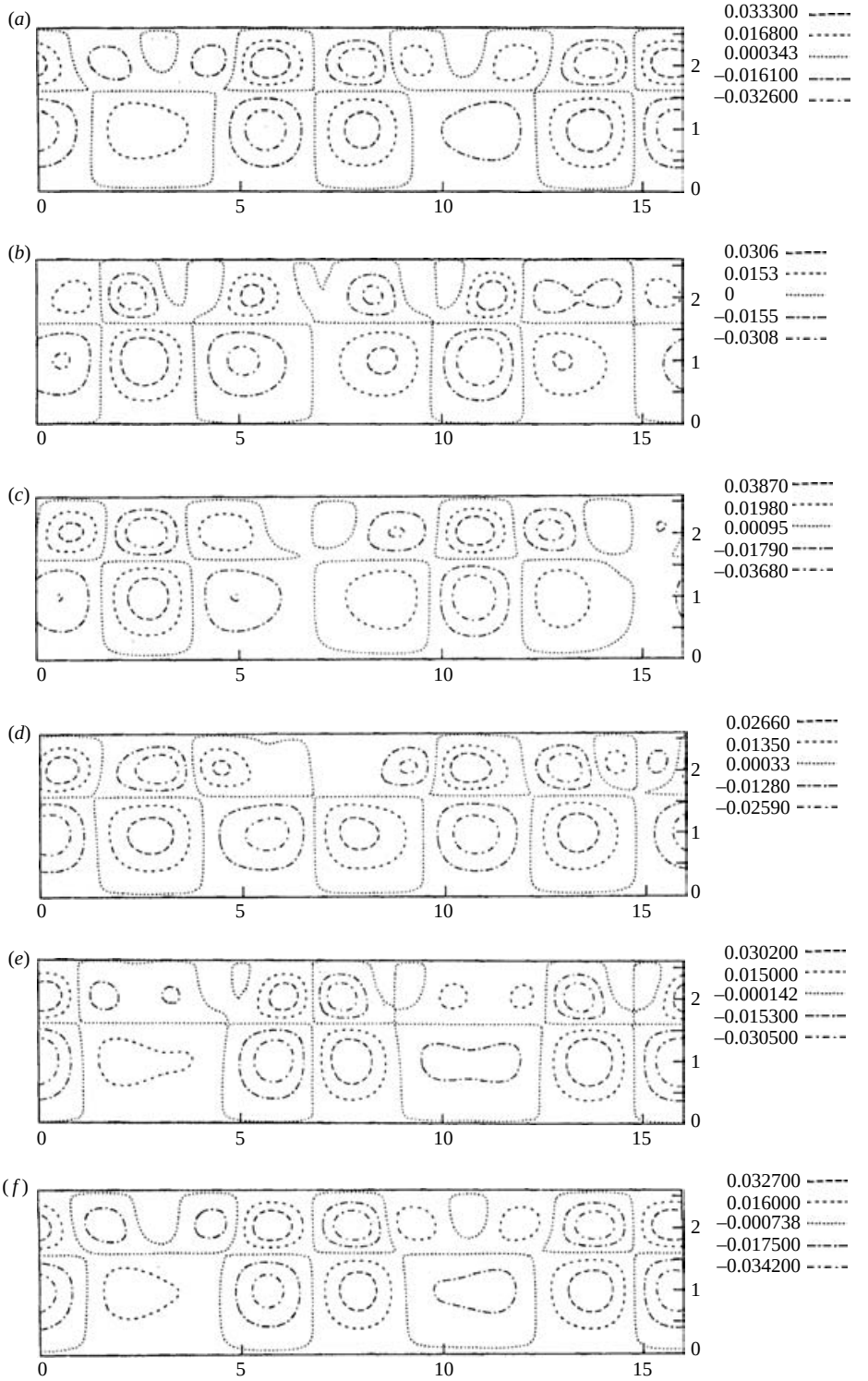


FIGURE 9(*a–f*). A time sequence of snapshots of streamlines for the oscillatory flow at $G = 89,\ K = 0.365,\ L = 16$.

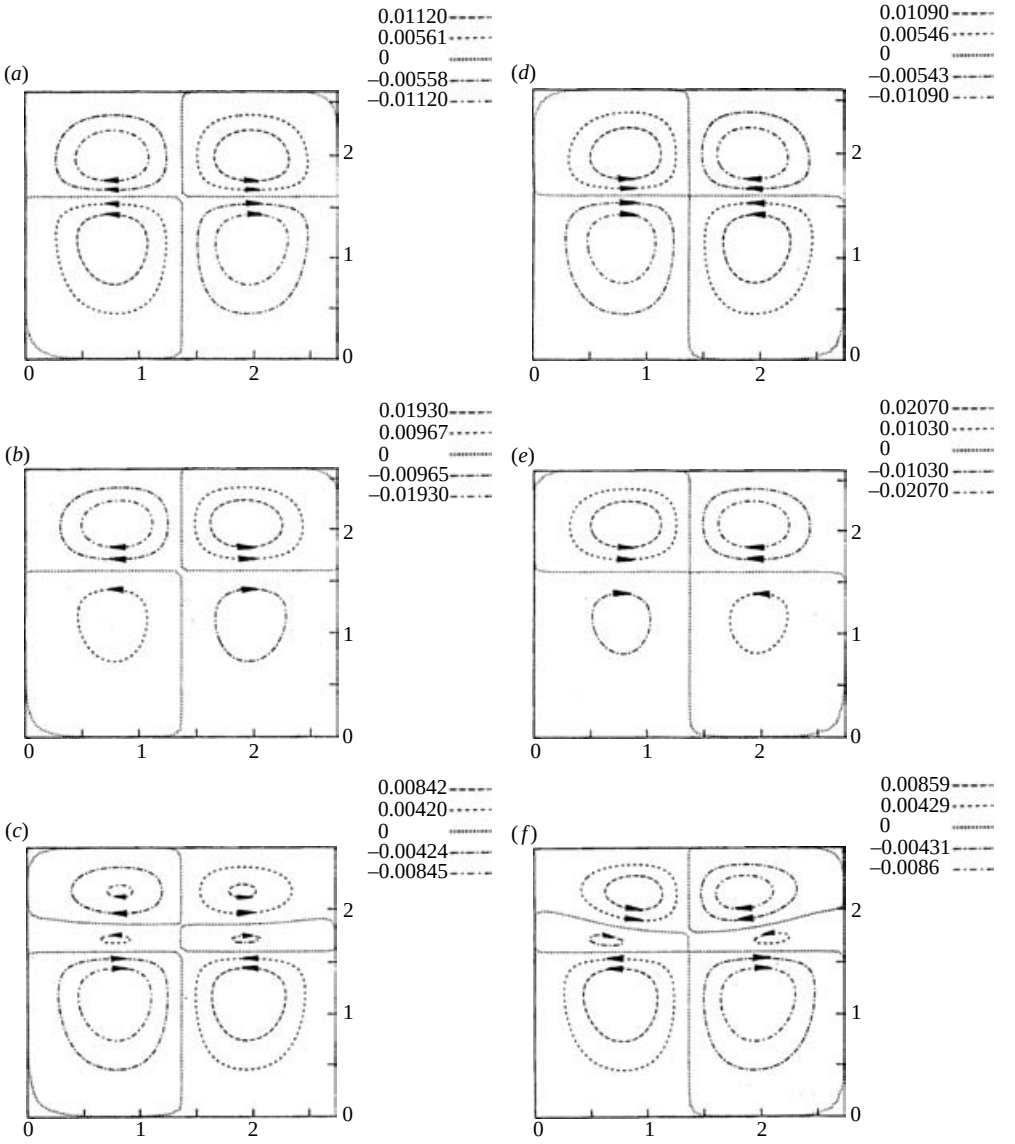


FIGURE 10(*a–f*). A time sequence of snapshots of streamlines for the symmetric time-periodic motion during one period for $G = 97$; $L = 2.74$.

As an example, let us consider the case $a = 1.6$, which corresponds to $r = 0.328$. It turns out that the minimum value of the Grashof number is achieved at the oscillatory branch of the neutral curve, if the inverse dynamic Bond number $K$ is inside a certain interval, $K_- < K < K_+$. The computations show that $K_- \approx 0.328$, and $K_+ \approx 0.411$, if $a = 1.6$ (the coincidence between values of $r$ and $K_-$ is casual). A typical neutral curve in the region $K_- < K < K_+$ is shown in figure 2.

Thus, though the fluid system under consideration does not reveal any oscillations in the absence of the thermocapillary effect, it is subject to an oscillatory instability when the latter effect is taken into account. In our opinion, that can give the explanation of the waves found by Degen *et al.* 1998. Taking a typical value $\alpha \sim 0.07$

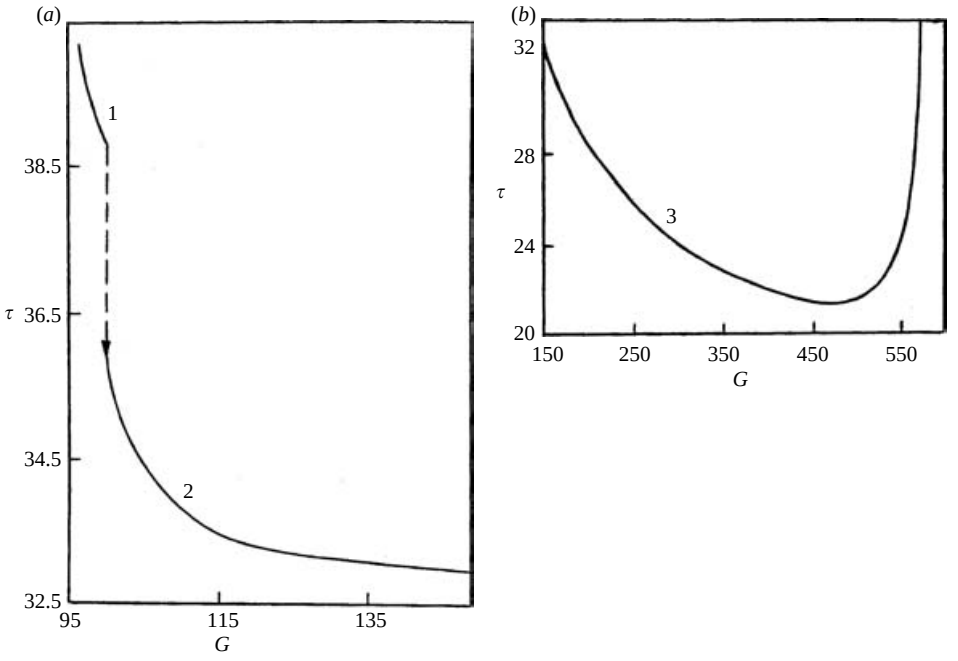


FIGURE 11. The dependence of the period of oscillations on the Grashof number for symmetric (line 1) and asymmetric oscillations (lines 2 and 3).

dyn cm$^{-1}$ K$^{-1}$ for a silicone oil (Degen *et al.* does not contain measurements of $\alpha$), we obtain $K = 0.33$, which is inside the interval where the observation of waves is predicted (Nepomnyashchy & Simanovskii 2004).

3.1.2. *Simulations in a short computational region*

A characteristic feature of the problem under consideration is the presence of two instability modes, an oscillatory mode (figure 2, line 3) and a monotonic mode (figure 2, line 4) with very close critical Grashof numbers. The interaction of these modes can produce complex flow regimes.

In the present subsection, we consider the spatially periodic oscillatory regimes generated solely by the oscillatory instability mode. In order to avoid the influence of the monotonic instability mode, we fix the period of the computational region $L = 2.74$, which corresponds to the critical wavelength of the oscillatory instability at $K = 0.4$.

The linear theory predicts the oscillatory instability, but it is unable to predict which kind of nonlinear regime, travelling waves or standing waves, will appear in the supercritical region.

In order to answer this question, we have used the periodic boundary conditions (20). We have found that above the threshold predicted by the linear stability theory, a travelling wave is developed (see figure 3):

$$\psi_m(x, z, t) = \psi_m(x - ct, z), \qquad T_m(x, z, t) = T_m(x - ct, z), \tag{25}$$

where $c$ is the phase velocity of the travelling wave. Certainly, travelling waves with opposite signs of $c$ are possible.

In the case of a travelling wave, the maximum and minimum values of stream-functions in both layers $\psi_{max,m} = \max \psi_m(x, z)$ $(m = 1, 2)$ are constant in time. For

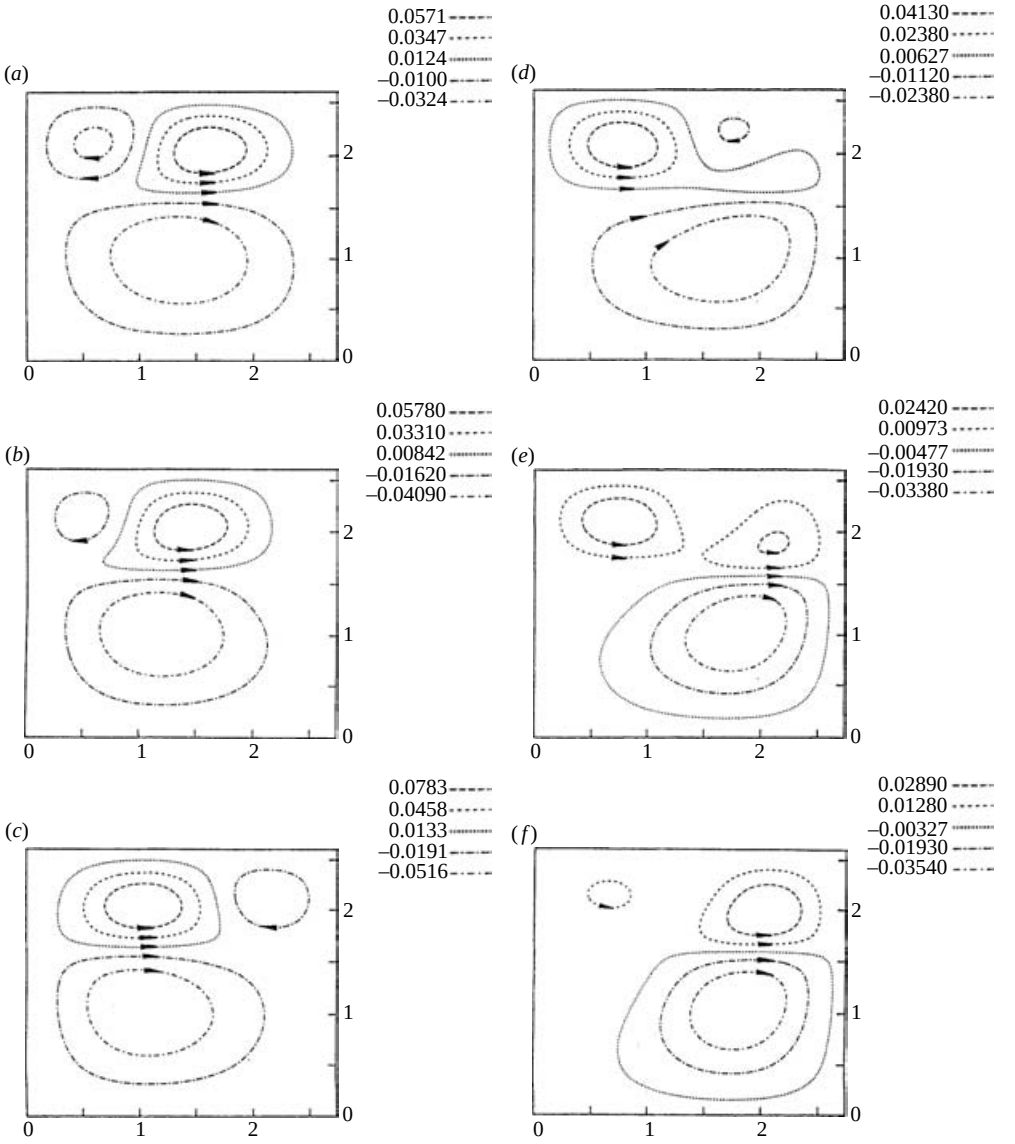


FIGURE 12(*a–f*). A time sequence of snapshots of streamlines for the asymmetric time-periodic motion during one period; $G = 102.16$; $L = 2.74$.

the wave moving to the left, the intensity of the positive vortex in the bottom fluid is slightly larger than that of the negative vortex.

With the increase of $G$, the period of oscillations grows (see figure 4), i.e. the phase velocity of waves decreases. This prediction coincides with the observations of Degen *et al.* (1998). When $G \geqslant 111$, the oscillatory motion disappears and the system is at steady state. The streamlines and isotherms, corresponding to the steady state are shown in figure 5.

According to the predictions of the linear theory, the oscillatory instability in an infinite two-layer system is replaced by a short-wave stationary instability (corresponding to line 1 of figure 2) at $K < K_-$ and by a long-wave stationary

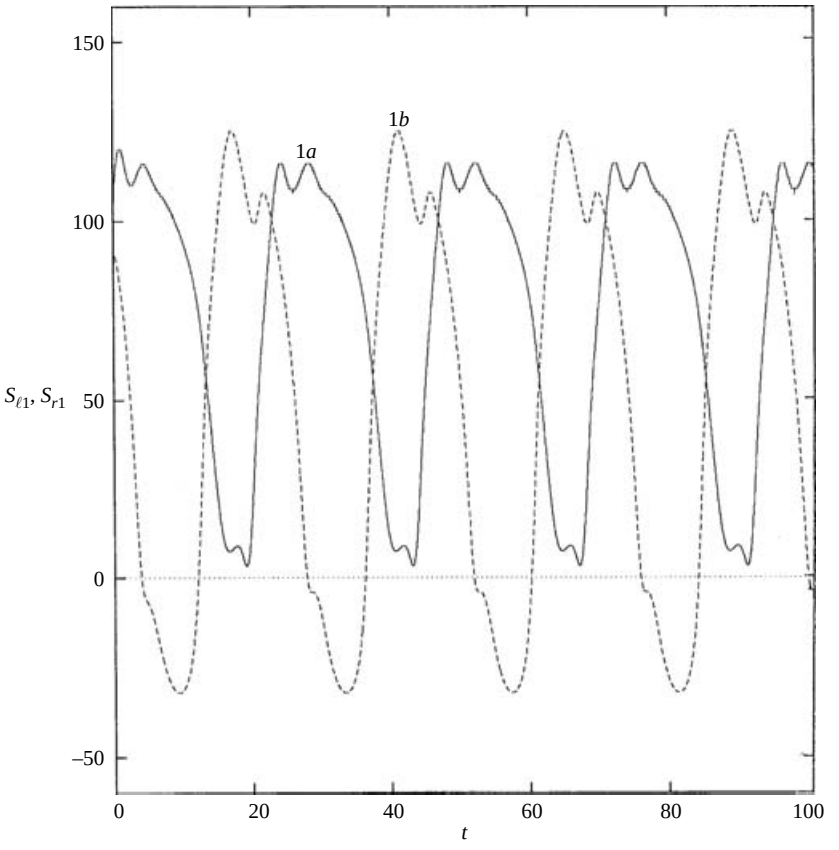


FIGURE 13. The dependences of $S_{l,1}$ (line 1$a$) and $S_{r,1}$ (line 1$b$) on time for $G = 302.16$.

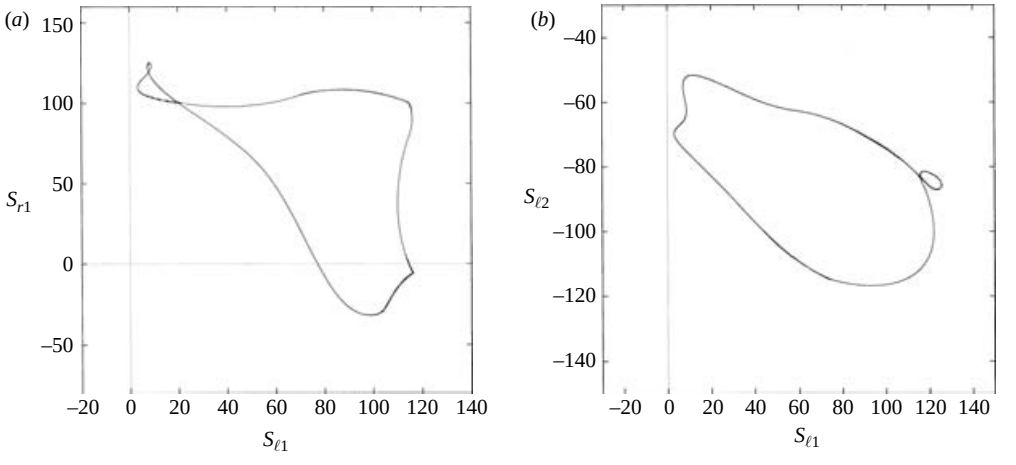


FIGURE 14. Phase trajectories for the asymmetric oscillations: ($a$)$S_{r1}(S_{l1})$; ($b$)$S_{l2}(S_{l1})$; $G = 302.16$.

instability (corresponding to line 4 of figure 2) at $K > K_+$. However, in a short computational region, the latter instability cannot appear. Therefore, we obtain travelling waves even for rather large values of $K$ (see figure 6) where the Marangoni effect is dominant.

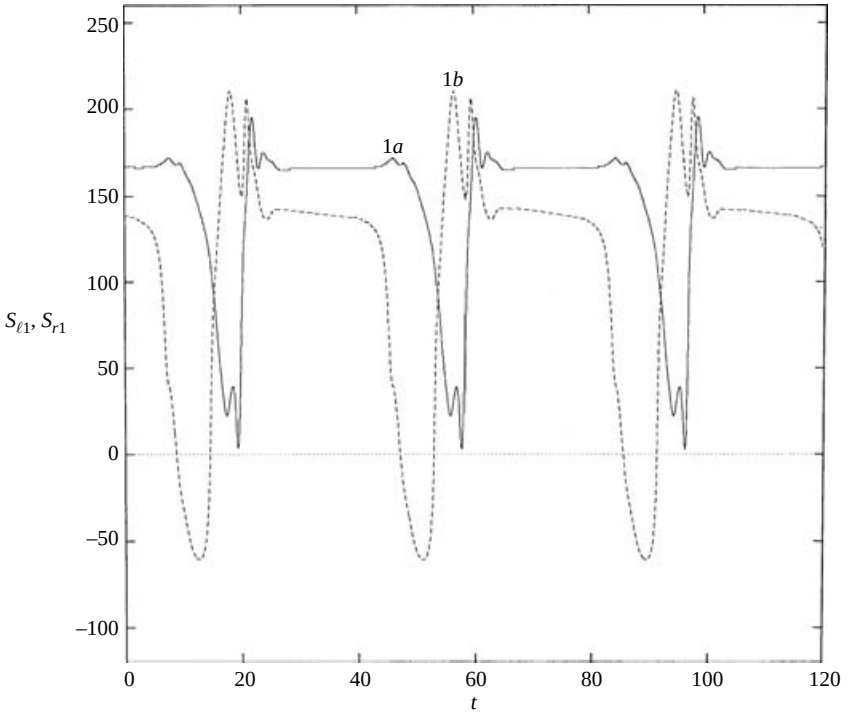


FIGURE 15. The dependences of $S_{l,1}$ (line 1$a$) and $S_{r,1}$ (line 1$b$) on time for $G = 573$.

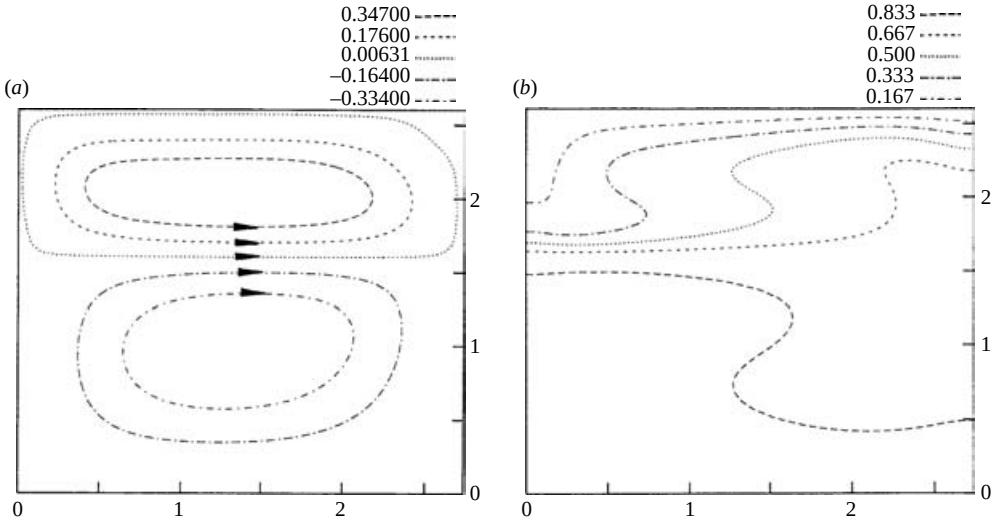


FIGURE 16. (*a*) Streamlines and (*b*) isotherms for the steady state ($G = 580$); $L = 2.74$.

3.1.3. *Simulations in long computational regions*

In a longer computational region ($L = 5.48$), the nonlinear flows are characterized by the interaction of two instability modes, a long-wave stationary mode corresponding to line 4 in figure 2, and a short-wave oscillatory mode corresponding to line 3 in figure 2. This interaction leads to a subcritical excitation of an oscillatory flow which can

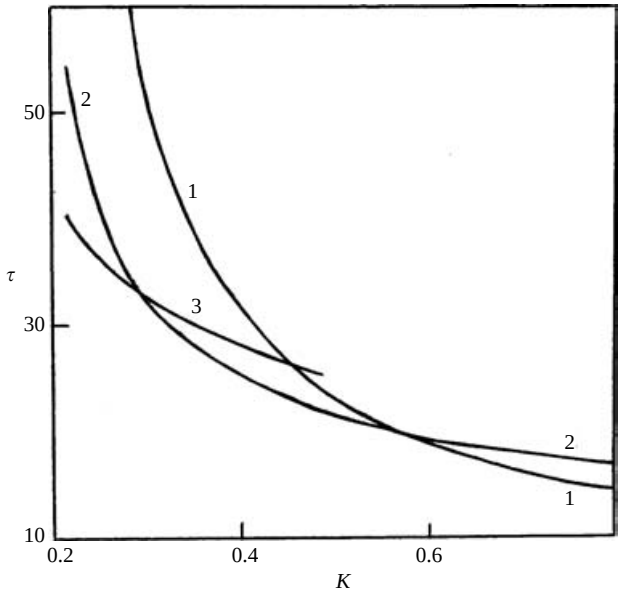


FIGURE 17. The dependence of the period of oscillations $\tau$ on the parameter $K$ for $G = 125$ (line 1), $G = 250$ (line 2) and $G = 575$ (line 3).

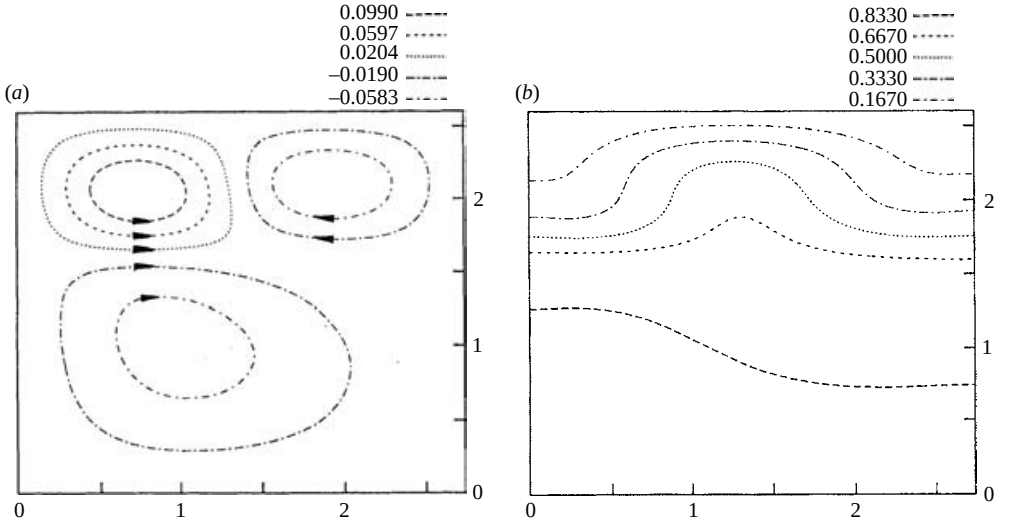


FIGURE 18. (*a*) Streamlines and (*b*) isotherms for the asymmetric steady flow; $G = 125$; $K = 0.19$.

be considered as a certain nonlinear superposition of a long-wave nearly stationary flow and a short-scale standing wave. This oscillatory regime is characterized by the symmetry properties

$$\psi_m(L - x, z, t) = -\psi_m(x, z, t), \qquad T_m(L - x, z, t) = T_m(x, z, t) \qquad (m = 1, 2), \quad (26)$$

and is observed in a wide interval of $G$, in both subcritical and supercritical regions. The snapshots of oscillations during half of the period are shown in figure 7.

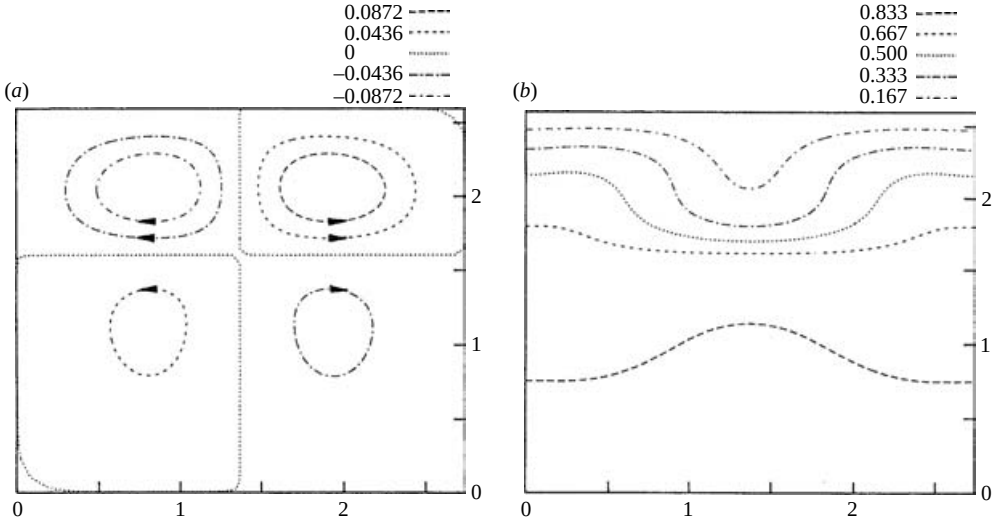


FIGURE 19. (*a*) Streamlines and (*b*) isotherms for the symmetric steady flow at the same values of parameters $G$ and $K$ as in figure 18.

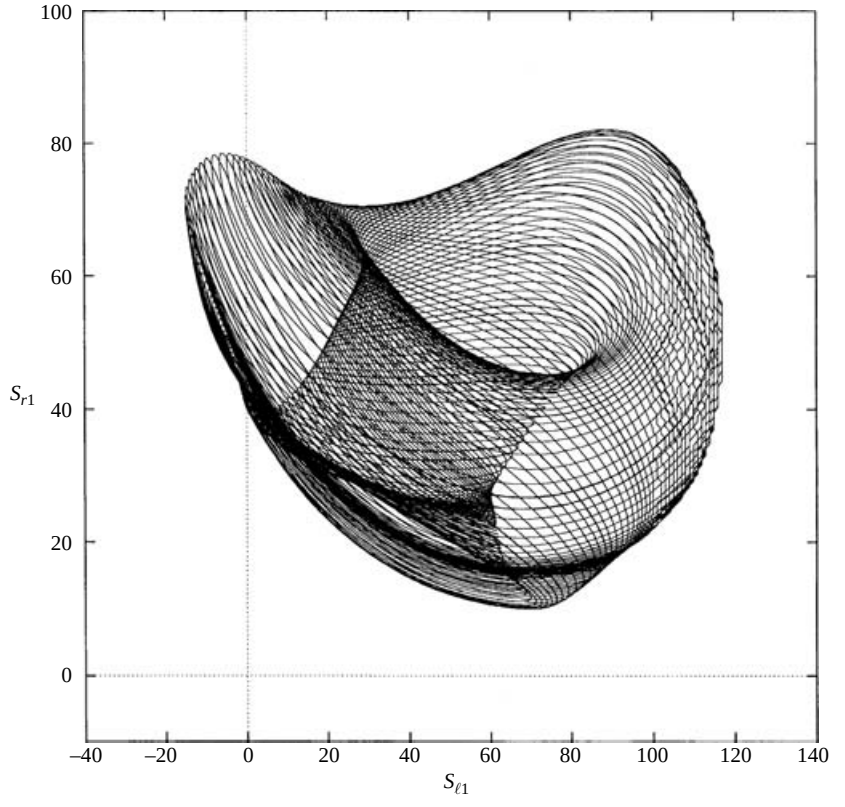


FIGURE 20. Phase trajectory in the plane $(S_{l1},\ S_{r1})$ for $G = 125;\ K = 10$.

In a narrow interval of $G$ around $G = 89$, we can obtain also another, asymmetric, kind of flow (figure 8) for the same values of parameters. The fields of streamfunctions for this flow contain some fragments resembling the corresponding fields for the

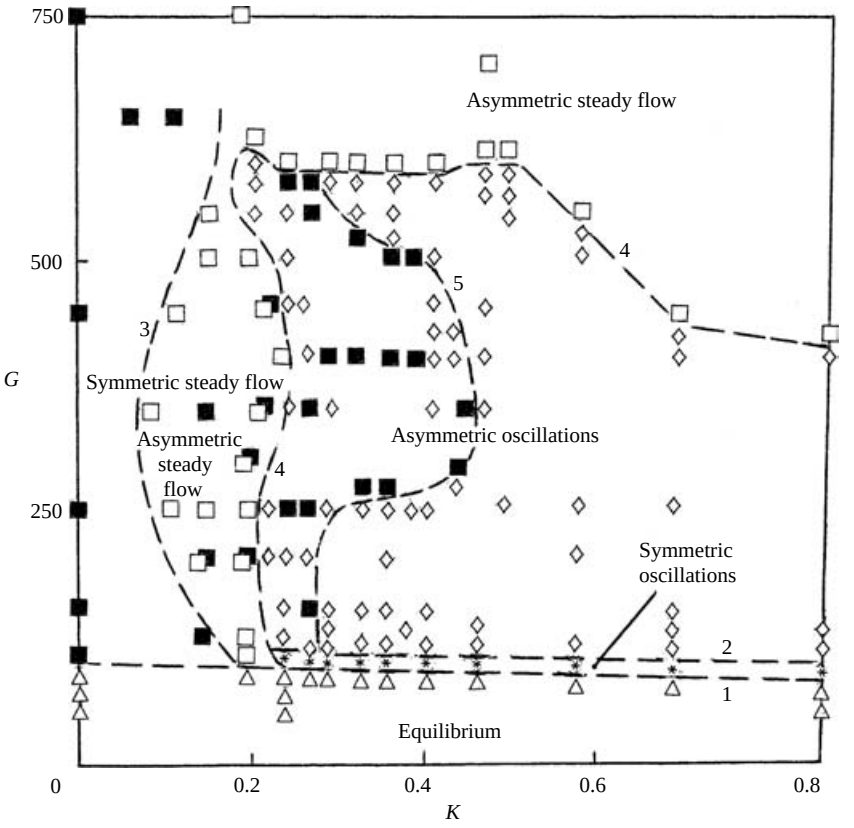


FIGURE 21. The general diagram of flow regimes in the plane ($K$, $G$). $\Delta$, equilibrium; $*$, symmetric oscillations; $\diamond$, asymmetric oscillations; $\blacksquare$, symmetric steady flow; $\square$, asymmetric steady flow. Line 1: upper boundary of the stability region of the equilibrium; line 2: transition between symmetric and asymmetric oscillations; line 3: left-hand boundary of the stability region of the asymmetric steady flow; line 4: transition between asymmetric oscillations and asymmetric steady flow; line 5: right-hand boundary of the stability region of the symmetric steady flow.

travelling wave. Nevertheless, there is no total motion of this structure during the period of oscillations. Below and above this interval, the asymmetric solution is unstable, and the system tends to a symmetric state.

Similar asymmetric periodic oscillations are observed in longer computational regions, but the spatial structure of the flow becomes more complicated (see figure 9). Note that dynamical regimes which combine stationary and oscillatory flow components were formerly studied in the problem of magnetoconvection with the depth-dependent ratio of ohmic to thermal diffusivity (Julien, Knobloch & Tobias 1999, 2000; see also Halford & Proctor 2002; Weiss 2002).

### 3.2. *Closed cavities*

#### 3.2.1. *Evolution of flow regimes by changing G*

To simulate the motions in a closed cavity, we used rigid heat-insulated boundary conditions (21) for $L = 2.74$. With the increase of the Grashof number, the mechanical equilibrium state becomes unstable and perfectly symmetric standing waves (type 1), satisfying symmetry conditions (26), are developed near the instability threshold.

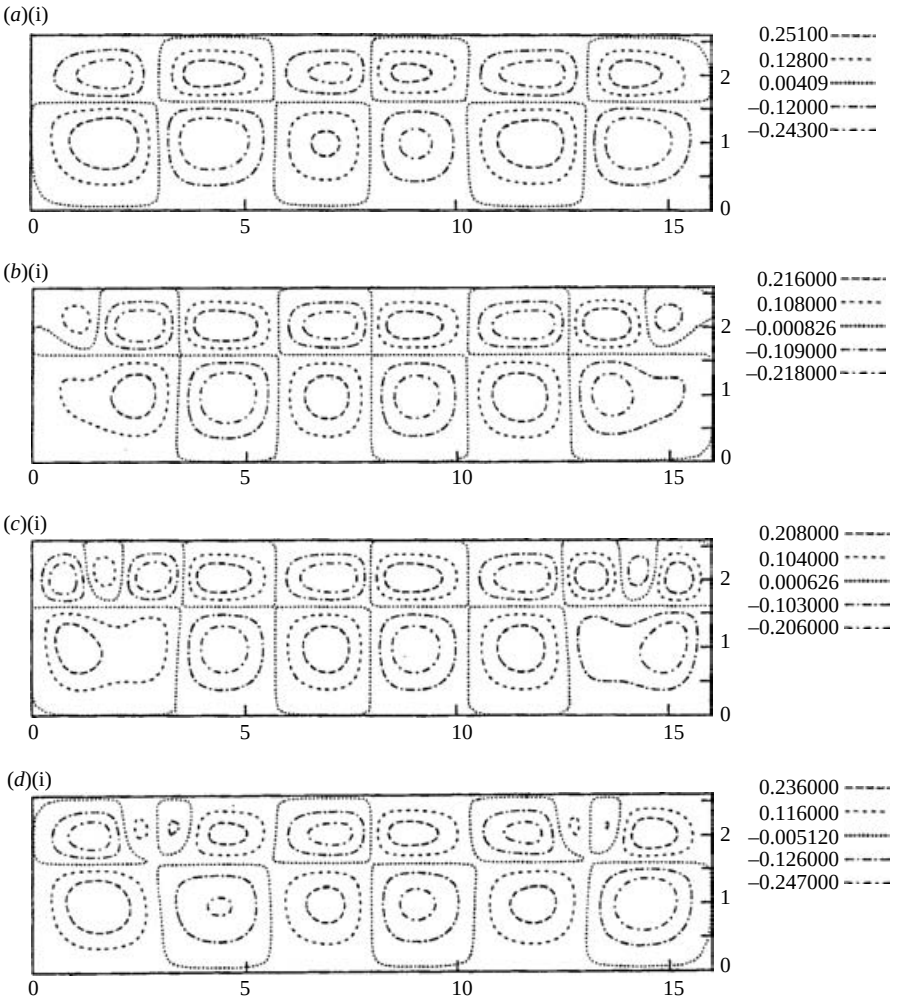


FIGURE 22. For caption see next page.

The snapshots of streamlines during one period of oscillations are presented in figure 10. The direction of the rotation is first changed in the bottom layer, and a two-store structure is produced in the top layer (figure 10*c*). Then, the vortices generated near the interface oust the 'main' vortices located in the upper part of the top layer (figure 10*d*). Thus, the direction of the vortices rotation is changed during half of the period (cf. figures 10*a* and 10*d*), and the process is repeated (figures 10*f*, 10*a*).

With the increase of the Grashof number, the period of oscillations decreases (see line 1 in figure 11). This type of symmetric oscillation takes place in the region $95.5 \leqslant G \leqslant 98.5$. When $G > 98.5$, the symmetric oscillations become unstable, and asymmetric oscillations (type 2) develop in the system. We failed to find any hysteresis between two types of oscillation. The snapshots of streamlines for this type of oscillation are presented in figure 12. The latter type of oscillation is characterized by the appearance of vortices of a relatively large horizontal size in the bottom layer. We can see, that for this type of oscillation the symmetry properties are violated.

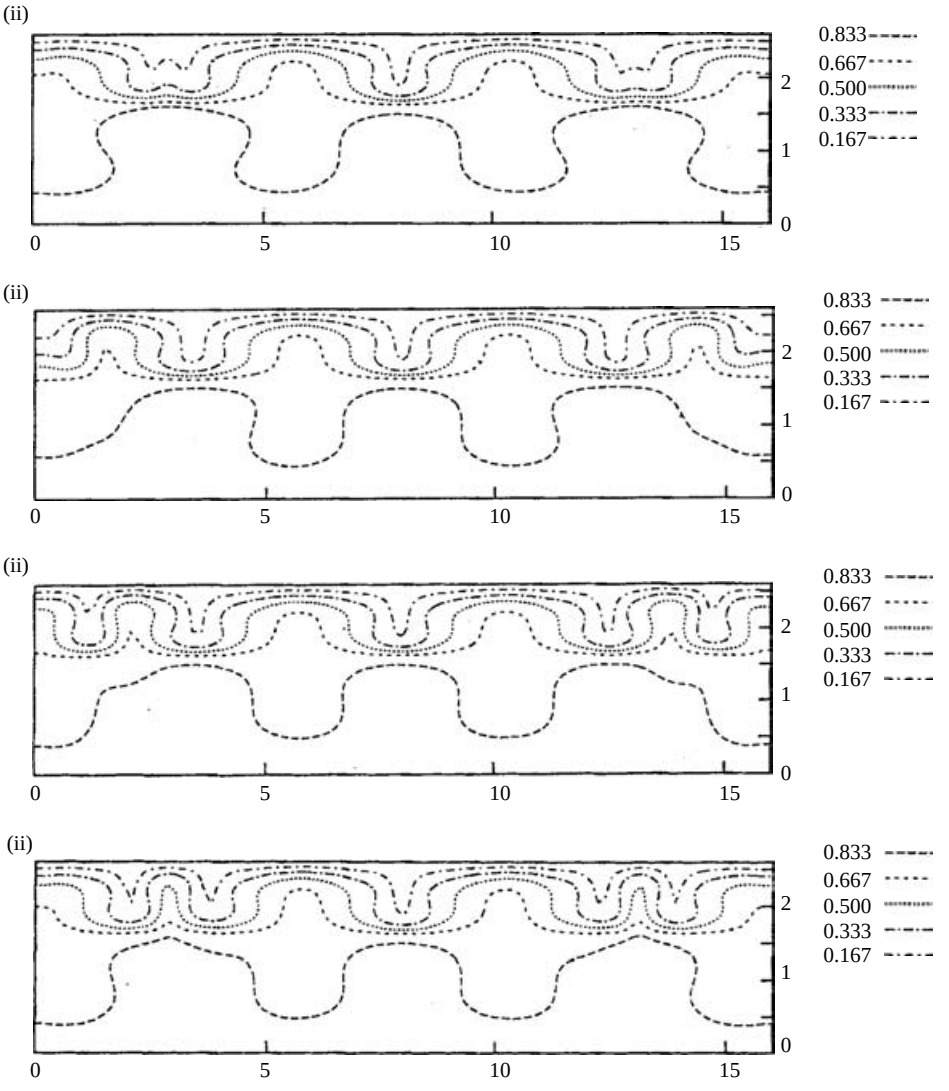


FIGURE 22. A time sequence of snapshots of (i) streamlines and (ii) isotherms for a symmetric oscillatory flow at $G = 101.3$, $K = 0.4$, $L = 16$.

At the larger values of $G$, the period of oscillations continues to decrease (line 2 in figure 11). When $G > 283$, the asymmetric oscillations become complicated.

In order to describe the time evolution of the solution, we use four integral variables defined in the following way:

$$S_{l1}(t) = \int_0^{L/2} \mathrm{d}x \int_a^{1+a} \mathrm{d}z \psi_1(x, z, t), \quad S_{r1}(t) = \int_{L/2}^{L} \mathrm{d}x \int_a^{1} \mathrm{d}z \psi_{1+a}(x, z, t), \tag{27}$$

$$S_{l2}(t) = \int_0^{L/2} \mathrm{d}x \int_0^{a} \mathrm{d}z \psi_2(x, z, t), \quad S_{r2}(t) = \int_{L/2}^{L} \mathrm{d}x \int_0^{a} \mathrm{d}z \psi_2(x, z, t). \tag{28}$$

Though these variables lack a clear physical meaning, they are sufficient for a qualitative understanding of the spatial structure of the flow (location of positive and negative vortices), the symmetry of the flow and the type of attractor.

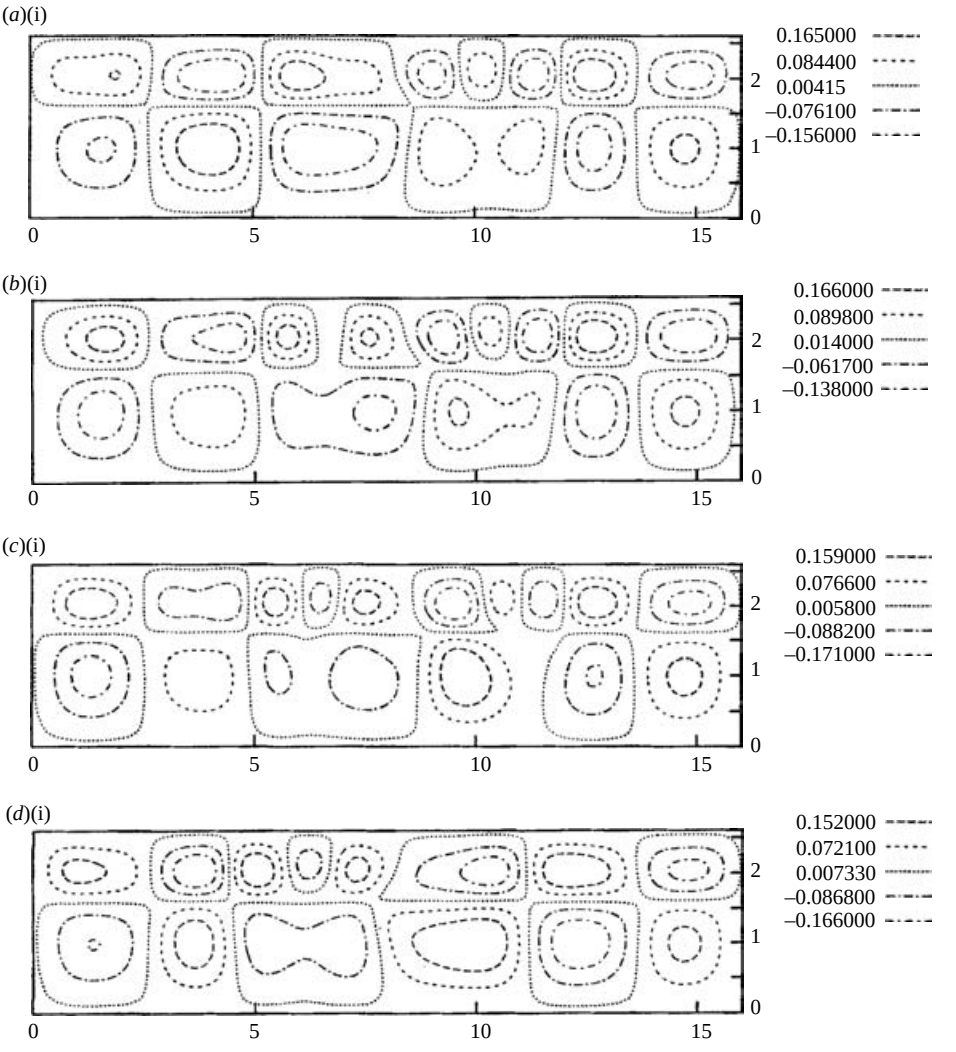


FIGURE 23. For caption see next page.

The dependences of $S_{l1}(t)$, $S_{r1}(t)$ $(m = 1, 2)$ and the corresponding phase trajectories are shown in figures 13 and 14. At $G > 475$, the period of oscillations grows rapidly (line 3 in figure 11). For both functions $S_{l1}(t)$, $S_{r1}(t)$ we observe a 'plateau' (see figure 15). With a further increase of $G$ the oscillations disappear. For $G$ close to $G_* = 576.5$, the period of oscillations $\tau$ satisfies the relation $\tau^{-2} \sim G_* - G$, which is characteristic for a saddle-node bifurcation. When $G > G_*$, the steady two-vortex motion takes place in the system. The streamlines and isotherms of the steady state are presented in figure 16.

It means that the oscillatory motion takes place in an interval of the Grashof number values bounded both from below – by the mechanical equilibrium state- and from above – by the steady state (see also Colinet & Legros 1994; Le Bars & Davaille 2002).

3.2.2. *Evolution of flow regimes by changing K*

Let us discuss now the influence of the inverse dynamic Bond number $K$ on the flow regimes for a fixed value of the Grashof number $G$ in a cavity with $L = 2.74$.

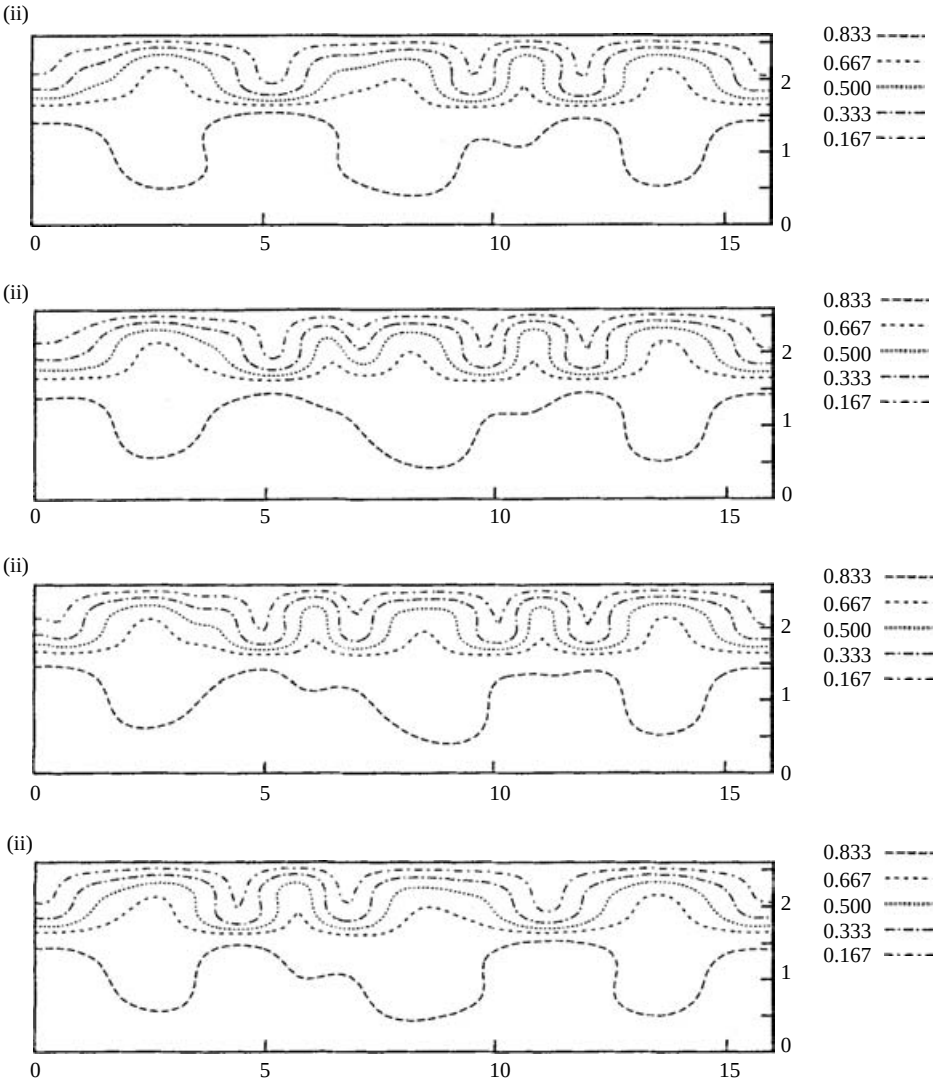


FIGURE 23. A time sequence of snapshots of (i) streamlines and (ii) isotherms for an asymmetric oscillatory flow at $G = 125$, $K = 0.4$, $L = 16$.

Recall, that for $a = 1.6$, $R_2 < R_1$ (see § 3.1.1). Therefore, the decrease of $K$ (weakening of the thermocapillary effect) makes the development of the stationary convection in the top layer more favourable. Indeed, with the decrease of $K$, the oscillations period increases (see figure 17), and finally, a steady asymmetric flow regime is developed (figure 18). If $K$ continues to decrease, we observe a transition into a symmetric flow with the intensity of motion in the top layer much stronger than that in the bottom layer (see figure 19). The stability region of the symmetric stationary flow overlaps with the stability regions of the asymmetric stationary flow and with that of the asymmetric oscillations.

The growth of $K$ is favourable for the development of the stationary instability in the bottom layer. However, the thickness of the bottom layer, and hence the

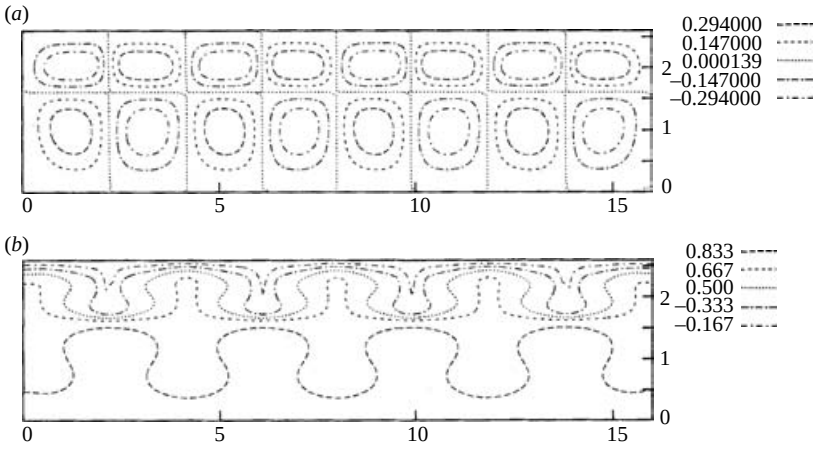


FIGURE 24. Snapshots of (*a*) streamlines and (*b*) isotherms for a stationary flow at $G = 410$, $K = 0.4$, $L = 16$.

characteristic size of bottom-layer convective cells, are significantly larger than the corresponding characteristics of the top layer. The cavity with $L = 2.74$ turns out to be too short for the development of steady bottom-layer convective cells. We performed simulations up to $K = 5.75$, and we did not observe any transitions from the oscillatory to the steady regimes with the growth of $K$. The period of oscillations decreases with the growth of $K$ (see figure 17). At $K \geqslant 4$, the periodic motion is replaced by an apparently quasi-periodic motion (see figure 20). The general diagram of regimes in the plane $(K, G)$ is shown in figure 21.

3.2.3. *Flow regimes in long cavities*

As in the case of long computational regions with spatially periodic conditions, the nonlinear regimes in long cavities are developed owing to the interaction of two instability modes, a stationary one and an oscillatory one. A typical flow contains a symmetric nearly stationary structure in the middle of the cavity, while some oscillations take place near the lateral boundaries (see figure 22). With the growth of $G$, the symmetry is broken (see figure 23). For sufficiently large $G$, a stationary flow is established (see figure 24).

## 4. Conclusion

The nonlinear development of the oscillatory instability in a two-layer system in the presence of buoyancy and thermocapillary effect, is investigated. Different types of boundary conditions on the lateral walls are used. It is shown that for the real system of fluids under the joint action of buoyancy and thermocapillary effects, the oscillatory instability may lead to different non-steady regimes. In the case of periodic boundary conditions, regimes of travelling waves and standing oscillations have been obtained. In the case of rigid boundary conditions, we observed symmetric and asymmetric standing waves. With the increase of the Grashof number, the period of oscillations increases in the case of periodic boundary conditions and changes non-monotonically in the case of rigid lateral walls. It is found that for both periodic boundary conditions and rigid heat-insulated lateral walls, the oscillatory motion is observed in a finite interval of the Grashof number values.

## REFERENCES


Busse, F. H. 1981 On the aspect ratios of two-layer mantle convection. *Phys. Earth Planet. Int.* **24**, 320–324.

Colinet, P. & Legros, J.-C. 1994 On the Hopf bifurcation occuring in the two-layer Rayleigh–Bénard convective instability. *Phys. Fluids* **6**, 2631–2639.

Colinet, P., Legros, J.-C. & Velarde, M. G. 2001 *Nonlinear Dynamics of Surface-Tension-Driven Instabilities*. Wiley.

Degen, M. M., Colovas, P. W. & Andereck, C. D. 1998 Time-dependent patterns in the two-layer Rayleigh–Bénard system. *Phys. Rev.* E **57**, 6647–6659.

Gershuni, G. Z. & Zhukhovitsky, E. M. 1982 On monotonic and oscillatory instability of a two-layer immiscible fluids system heated from below. *Sov. Phys. Dokl.* **27**, 531.

Gilev, A. Yu., Nepomnyashchy, A. A. & Simanovskii, I. B. 1987 Onset of the oscillatory thermogravitational convection in a two-layer system when heating from below. *Dynamics of Viscous Fluids, Sverdlovsk* 36–37 (in Russian).

Halford, A. R. & Proctor, M. R. E. 2002 An oscillatory secondary bifurcation for magnetoconvection and rotating convection at small aspect ratio. *J. Fluid Mech.* **467**, 241–257.

Julien, K., Knobloch, E. & Tobias, S. 1999 Strongly nonlinear magnetoconvection in three dimensions. *Physica* D **128**, 105–129.

Julien, K., Knobloch, E. & Tobias, S. 2000 Nonlinear magnetoconvection in the presence of strong oblique fields. *J. Fluid Mech.* **410**, 285–322.

Kuskova, T. V. & Chudov, L. A. 1968 On approximate boundary conditions for vortex at calculation of the flows of viscous incompressible fluid. *Comput. Meth. Programming* **11**, 27 (in Russian).

Le Bars, M. & Davaille, A. 2002 Stability of thermal convection in two superimposed miscible viscous fluids. *J. Fluid Mech.* **471**, 339.

Liu, Q. S., Zhou, B. H. & Tang, Z. M. 2004 Oscillatory instability of Rayleigh–Marangoni–Bénard convection in two-layer liquid system. *Abstracts of International Marangoni Association Congress (IMA – 2), Bruxelles, Belgium.*

Nepomnyashchy, A. A. & Simanovskii, I. B. 2004 Influence of thermocapillary effect and interfacial heat release on convective oscillations in a two-layer system. *Phys. Fluids* **16**, 1127–1139.

Rasenat, S., Busse, F. H. & Rehberg, I. 1989 A theoretical and experimental study of double-layer convection. *J. Fluid Mech.* **199**, 519–540.

Renardy, Y. Y. 1996 Pattern formation for oscillatory bulk-mode competition in a two-layer Bénard problem. *Z. angew. Math. Phys.* **47**, 567–590.

Renardy, Y., Renardy, M. & Fujimura, K. 1999 Takens–Bogdanov bifurcation on the hexagonal lattice for double-layer convection. *Physica* D **129**, 171.

Simanovskii, I. B. 1979 Finite-amplitude convection in a two-layer system. *Fluid Dyn.* **14**, 637–642.

Simanovskii, I. B. & Nepomnyashchy, A. A. 1993 *Convective Instabilities in Systems with Interface*. Gordon and Breach.

Weiss, N. O. 2002 Umbral and penumbral magnetoconvection. *Astron. Nache.* **323**, 371–376.